

Bidirectional Catalysis Disintegration and Mineral Polymerization via Endogenous Iron(III) from Iron-Rich Sludge in Synergy with Waste Incineration Fly Ash

Dongjie Pang, Yanpeng Mao,* Yang Jin, Jiazheng Zhang, Jingyi Dong, Xujiang Wang, Jingwei Li, and Wenlong Wang



Cite This: *ACS Omega* 2023, 8, 34663–34677



Read Online

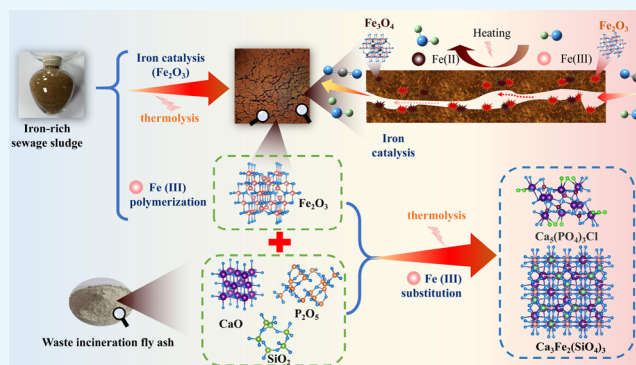
ACCESS |

Metrics & More

Article Recommendations

Supporting Information

ABSTRACT: To enhance the utilization of solid waste in cement kiln co-processing, this study analyzed the multifaceted synergy of pyrolysis and mineralization processes of iron-rich sludge (SS) and waste incineration fly ash (FA) at optimal blending ratios. Based on the physicochemical properties of SS and co-pyrolysis experiments, it was found that Fe acted as a positive catalyst in pyrolysis between 700 and 1000 °C, while the endogenous polymerization effect of Fe(III) mineral groups dominated above 800 °C. Additionally, the study investigated the solidification and migration of heavy metals and the transformation of harmful elements (S, Cl, and P). Results indicated that the best mixture ratios for SS and FA were 6:4 and 9:1, respectively, and synergistic pyrolysis and mineral co-curing effects were observed in the pyrolysis temperature range of 50–1000 °C. The synergy between SS and FA allowed for the decomposition and solidification of harmful organic components and heavy metals, reducing environmental risks. Furthermore, in actual production, by mixing 100 tons of SS and FA with Portland cement with a daily output of 2500 tons, the compressive strength during early hydration stages can reach 34.52 MPa on the third day, exceeding the highest performance of Portland cement (62.5R) strength index specified in the standard.



1. INTRODUCTION

Sewage treatment with ferric flocculant results in complex, iron-rich sewage sludge (SS), which carries microbial infections, organic contaminants, and heavy metals.¹ This sludge becomes a hotbed for the majority of organic pollutants and biological pathogens during the wastewater treatment process. If not properly disposed of, it presents significant environmental risks, such as water eutrophication, red tides, and water pollution, due to its high concentrations of nitrogen, phosphorus, and sulfur.² Moreover, heavy metals in the wastewater can precipitate or adsorb onto the sludge, eventually entering the ecological chain and threatening both the ecosystem and human health.³ Furthermore, improper sludge disposal emits foul odors harmful to the human respiratory system and causes air pollution.⁴ Furthermore, inadequate sludge disposal may lead to the emission of foul odors, affecting the human respiratory system and causing air pollution. Therefore, a low-carbon solution for sludge disposal is paramount. Researchers have developed various pyrolysis disposal processes, such as fluidized bed pyrolysis, decomposer gasification, and hydrothermal carbonization, to this end. Cement kilns,⁵ however, offer a comprehensive solution, fully degrading harmful organic compounds and solidifying heavy metals in the sludge to minimize their environmental impact.

This process involves the precipitation and physical encapsulation of these heavy metals by silicate compounds, such as calcium silicate.⁶

The co-treatment of sludge in cement kilns is gaining worldwide attention as an environmentally friendly disposal method, given the growing amount of sludge production.⁷ Furthermore, the similarity between the building material components of cement and sludge offers additional advantages. SS possesses specific characteristics, including a calorific value and raw materials like CaO, SiO₂, and Al₂O₃, making it suitable as a fuel and raw material in cement manufacturing.⁸ Thus, utilizing sludge in cement production allows for resourceful reuse and contributes to sustainable practices.⁹ However, untreated solid waste like sludge can negatively impact the quality of cement clinker and lead to kiln damage due to the accumulation of hazardous materials.¹⁰ Therefore, proper

Received: May 23, 2023

Accepted: August 30, 2023

Published: September 15, 2023



Table 1. Physicochemical Properties of the SS and FA (Air-Dried Basis)^{a,b,c,d}

| proximate analysis | content (wt %) | | ultimate analysis | content (wt %) | |
|--------------------|----------------|-------|-------------------|----------------|--------|
| | SS | FA | | SS | FA |
| moisture | 4.85 | 4.2 | C | 36.74 | 2.06 |
| volatile | 36.51 | 9.89 | H | 5.97 | 1.21 |
| ash | 54.62 | 84.22 | N | 2.75 | <0.005 |
| fixed carbon | 4.02 | 1.69 | S | 0.94 | 1.56 |
| | | | O | 23.15 | 6.75 |

| compositions | content (wt %) | | heavy metals concentration | content (wt %) | |
|--------------------------------|----------------|-------|----------------------------|----------------|---------|
| | SS | FA | | SS | FA |
| Fe ₂ O ₃ | 48.26 | 7.24 | As | 93.44 | 50.95 |
| CaO | 11.99 | 34.79 | Zn | 14,123.98 | 3764.88 |
| P ₂ O ₅ | 10.45 | 2.47 | Cd | 0.98 | 66.32 |
| SiO ₂ | 10.2 | 24.7 | Ni | 335.63 | 118.21 |
| Al ₂ O ₃ | 9.21 | 8.23 | Mn | 4305.12 | 1091.73 |
| SO ₃ | 2.33 | 7.49 | Cr | 260.83 | 863.68 |
| MgO | 1.10 | 2.79 | Cu | 334.64 | 1123.77 |
| Cl | 0.74 | 5.48 | Pb | <0.01 | 765.16 |
| K ₂ O | 0.59 | 2.16 | | | |
| Na ₂ O | <0.001 | 1.2 | | | |

^aO, calculated by difference (O% = 100% - C% - H% - N% - S% - moisture% - ash%). ^bFixed carbon, calculated by difference (fixed carbon% = 100% - moisture% - volatiles% - ash%). ^cMetal chlorides in waste incinerator fly ash are primarily in the form of NaCl and KCl. ^dThe detection limit of heavy-metal ions was 0.01 to 10 mg/L.

pretreatment of sludge is a critical step toward sustainable resource utilization.¹¹

The waste heat generated during cement kiln production can be effectively utilized as a sludge disposal terminal, as the pyrolysis pretreatment process should be closely integrated with the cement kiln production process. The tertiary air temperature in the grate cooler used for clinker cooling can reach temperatures between 810 and 1000 °C, providing an ideal heat source for high-temperature sludge pretreatment and removal processes, ensuring the sludge reaches pre-harmful levels.¹² Simultaneously, cement kilns are commonly used for the disposal of mixed solid waste from various sources, extending beyond sludge alone. For example, waste incineration fly ash (FA) with a high CaO concentration can be a substitute raw material for cement production.¹³ The synergistic characteristics of FA for combined use with the SS of wastewater were further investigated because FA since FA has the ability to facilitate quality in wastewater disposal.¹⁴ However, the presence of chloride ions, sulfate ions, and alkali metal ions in FA imposes limitations on the proportion of raw material substitution.¹⁵ During the preheating process, inorganic chlorine in FA is gradually released and some metallic chlorides evaporate, contributing to the desired removal effect.¹⁶ To manage these complexities, the shredding–mixing–pumping (SMP) system plays a crucial role. It is designed to convert semisolid and solid materials with varying water content, poor flowability, uneven physical and chemical characteristics, and impurities into a uniform, flowable slurry. This system facilitates the co-disposal of cement in cement kilns with hazardous waste and aids in hazardous waste management.¹⁷ It incorporates FA combined with a dry SS disposal option for municipal sewage. In addition, the simultaneous disposal of FA and SS has the benefit of solidifying heavy metals. According to previous studies, iron phase flocculants applied to the SS treatment process result in SS being rich in Fe₂O₃. Although FA is rich in CaO, SiO₂, and Al₂O₃, it can immobilize heavy metals.¹⁸ Thus, the

simultaneous disposal of SS and FA successfully immobilizes heavy metals without requiring additional additives.¹⁹ Previous studies have shown that adding iron-containing chemicals and combining SS and FA in different ratios during pyrolysis can effectively immobilize heavy metals.²⁰ As a corollary, a critical problem in cement kiln co-disposal using FA technology has emerged to determine the ideal ratio of co-pretreatment of SS and FA through trials.²¹

This study seeks to increase the proportion of waste incineration fly ash (FA) and sewage sludge (SS) that can be used as feedstock in cement kilns. To mechanistically investigate the catalytic principle of endogenous iron pyrolysis and polymerization principle of endogenous iron mineral formation, the pyrolysis characteristics of SS with various FA mixing ratios and their synergistic inhibition effects were studied. Additionally, the co-processing ratio of SS and FA was investigated by thermogravimetric-Fourier transform infrared spectroscopy (TG-FTIR) to determine the ideal co-processing ratio for safe and sustainable co-processing of SS and FA in cement kilns. At the same time, X-ray diffraction (XRD) was used to compare the ideal mixing ratio with the mineral changes of pure SS and FA at the same disposal temperature.

2. MATERIALS AND METHODS

SS was obtained from Everbright Water (Zibo) Holdings Limited in Shandong Province, China. Sedimentation–anaerobic digestion–Fenton oxidative degradation is the method used by the business to dispose of its wastewater. Fe(OH)₃ colloid was formed after FeCl₃ was added as a flocculant, and the final precipitated substrate mixture was the initial test sample for this experiment. FA was gathered from Zibo Green Energy Co., Ltd. in Shandong Province, China. The business used a two-stage screw conveyor to transport the municipal waste to the incinerator, where it was burned in the fluidized bed. In order to collect the FA samples used in this experiment, the fly ash produced after waste incineration was collected from the flue gas purification system, cooled to below

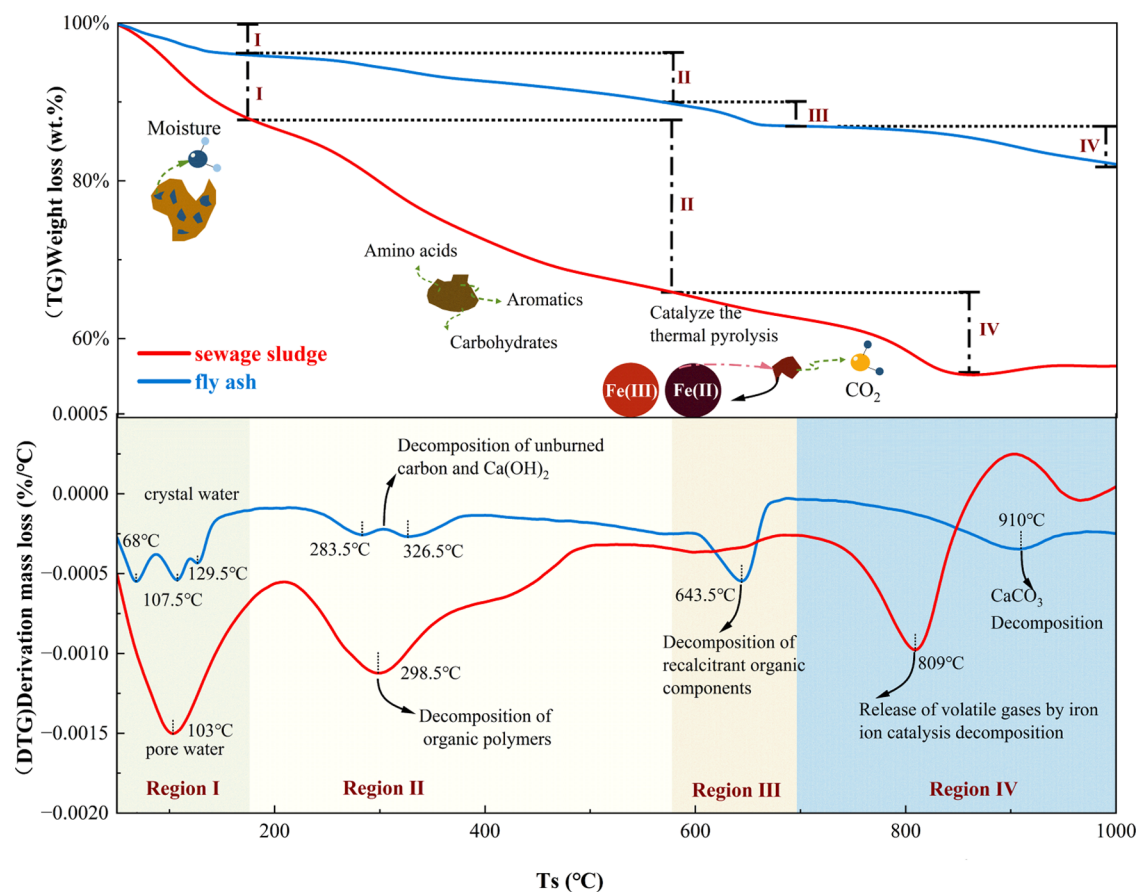


Figure 1. TG and DTG curves of the SS and FA at the heating rate of 10 K/min.

100 °C through a cooler, and stored in a storage silo. The two types of samples were dried at 105 °C for 24 h in a vacuum drying oven (DHG-90140AD, China). Before the experiment, the two materials were crushed using a mixer (JM-100, China) for 5 min, respectively, and were mixed and stirred for 10 min. For our laboratory experiments, all of the SS and FA pellets were powder-milled and sieved to derive particles <2 mm in diameter. Dry SS powder and FA powder were mixed according to a 5% unit mixing increment of FA, from 95% (SS/FA = 9.5:0.5) named SS95 to 55% (SS/FA = 5.5:4.5) named SS55.

The chemical compositions and the mineral phases of SS and FA were analyzed by ultimate, proximate analyses, benchtop powder X-ray diffraction (XRD), and X-ray fluorescence spectrometry (XRF), respectively. The levels of heavy metals (As, Zn, Cd, Ni, Mn, Cr, Cu, Pb), were analyzed after acid digestion. SS and FA samples (0.1 g) were placed in a 100 mL microwave digestion tube, respectively. 2 mL of HF and 10 mL of aqua regia were prepared with HNO₃ and HCl at a volume ratio of 1:3. The mixture was heated on a microwave dissolver (TANK40; SINEO, Shanghai, China) to complete dissolution and was readjusted to the same proportion. These steps were repeated until the liquid became light yellow and the precipitate disappeared. Metal concentrations were analyzed by inductively coupled plasma (ICP) (ICPS-8000; Shimadzu, Kyoto, Japan). All analyses were performed in duplicate or triplicate and average values were calculated. The physicochemical properties of raw SS and FA are shown in Table 1.

TG analysis experiments on SS, WW, and their mixtures were carried out in a TG analyzer (TGA8000, PerkinElmer). All experiments were carried out at a flow rate of 50 mL/min under an N₂ atmosphere to reduce the error of heat transfer. The samples were heated from 50 °C to 1000 °C at a heating rate of 10 K/min. In each experiment, the mass of the sample was maintained at 8 ± 0.5 mg to ensure the reference ability of pyrolysis. Multiple trials were performed until the maximum standard deviation of the three TG curves was less than 5% and the average data was used. In order to better characterize the synergistic performance of the thermal treatment of FA on SS and the performance of the degree of pyrolysis carried out, the co-pyrolysis performance assessment parameter CPI and the pyrolysis synergistic characterization parameter ΔW were therefore introduced with different blending ratios as independent variables.²²

Through the molecular and denominator parameters of eq 1, the degree of pyrolysis difficulty is represented by the CPI, which represents the comprehensive pyrolysis index. The initial decomposition temperature, duration, and maximum rate of the pyrolysis process all have a significant impact on the value of CPI. A more intense pyrolysis reaction is indicated by high values of CPI, which can be seen that a higher CPI means that pyrolysis is easy to carry out. Therefore, CPI can reflect the performance of pyrolysis.

$$\text{CPI} = \text{DTG}_{\text{max}} \cdot \text{DTG}_{\text{mean}} \cdot M_{\infty} / T_i \cdot T_p \cdot \Delta T_{1/2} \quad (1)$$

where T_i (°C) is the initial decomposition temperature; T_p (°C) is the temperature with the highest mass loss rate; M_{∞} (%) is the co-pyrolysis mass loss amount mass (100%—the

residual mass percentage); DTG_{\max} (%/min) is the maximum mass loss rate; and DTG_{mean} (%/min) is the average mass loss rate. When $DTG_{\text{momentary}}/DTG_{\max} = 1/2$, $\Delta T_{1/2}$ is the temperature value corresponding to $DTG_{\text{momentary}}$ (this temperature value occurs before the maximum weight loss rate).

The synergistic or inhibitory effect between FA and SS was investigated from the perspective of weightlessness. The difference between the calculated TG value and the experimental TG value of the mixture can be expressed by eqs 2 and 3.²³

$$\Delta W = TG_c - TG_e \quad (2)$$

$$TG_c = xSS \cdot TG_{SS} + (1 - x)SS \cdot TG_{FA} \quad (3)$$

where ΔW is the degree of synergy or inhibition, TG_e (%) is the experimental thermogravimetric value, TG_c (%) is the theoretically calculated thermogravimetric value, and x is the blending ratio.

This is followed by a discussion of the TG-FTIR technique for the analysis of fugitive gases from the co-pyrolysis of SS with FA. A Fourier infrared (FTIR) spectrometer (Spectrum Two, PerkinElmer) was used to analyze the organic compounds released during SS and FA heating in the range of 500–4000 cm^{-1} .

The chemical compositions of the materials were analyzed by X-ray fluorescence spectrometry (XRF; Thermal Scientific PW4000). The mineral phases of the materials were demonstrated via an X-ray diffractometer (XRD; Rigaku Dmax-2500PC, Japan), which was operated at 50 kV and 100 mA, as well as a scanning speed of 2.4°/min over a range of 10–80°. And the sample disk was rotated at 1 rps to obtain accurate diffraction data. The sample disk was rotated at 1 rps to obtain accurate diffraction data. The original sample and the mixture were observed for changes in minerals at different temperature backgrounds to determine whether the sample at the optimum blending ratio adds beneficial mineral composition to the cement raw meal from a solid-phase perspective.

3. RESULTS AND DISCUSSION

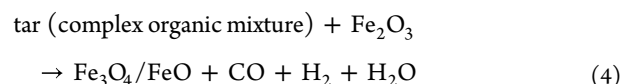
3.1. Comparison of the Pyrolysis Processes of SS and FA. 3.1.1. TG Analysis of Microgravity Thermal Processes.

The pyrolytic characteristics of two types of solid waste, sewage sludge (SS) and fly ash (FA), were examined through TG-DTG analysis, as shown in Figure 1. Notable differences in the microgravity changes during pyrolysis were observed due to the varying organic matter content in SS and FA. For FA, pyrolysis occurred in four stages across the temperature range of 50–1000 °C. The initial stage involved removing interstitial and crystallization water below 175 °C. The next stage, spanning 175–576 °C, encompassed thermal decomposition of $\text{Ca}(\text{OH})_2$, volatilization of inherent crystalline water, and combustion of unburned carbon.²⁴ The third stage, within the 576–695 °C range, focused on the pyrolysis of resistant organic components. Finally, the decomposition of CaCO_3 occurred at 830 °C. In contrast, SS pyrolysis occurred over three stages within the same temperature range. The first stage was dedicated to the removal of internally bound water via dehydration below 175 °C. The second stage, between 175 and 576 °C, involved pyrolysis and volatilization of organic matter. Notably, around 298.5 °C, aliphatic compounds in SS are predominantly converted into water, noncondensable gas, and tar. Beyond 350 °C, proteins underwent pyrolysis,

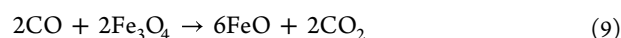
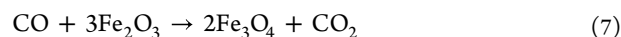
decomposing into smaller molecular compounds through peptide bond cleavage.²⁵ Lastly, the release of volatile gases due to the catalytic reaction of internal iron defined the third stage, at temperatures above 576 °C.

The TG-DTG curves revealed distinct weight loss patterns during initial and subsequent stages. The weight loss during the water removal and organic matter volatilization stages of SS was more considerable than that of FA. The complete volatilization of organic matter in SS took place before the temperature reached 511 °C. Despite pre-drying the samples for the TG experiment, a substantial change in water loss was still noticeable in SS. This suggests that the moisture content of SS arises not only from external sources but also from interstitial water and compound-bound water within the SS macromolecules, leading to a swift weight loss during the dewatering stage. Theoretically, FA, being a high-temperature incineration byproduct, should not contain moisture. Nevertheless, due to the strong hygroscopicity of abundant CaO and some CaSO_4 in the ground FA powder, significant weight loss was noted during the initial and subsequent stages.

The pyrolysis process of SS becomes complex in the second and third stages. At approximately 200 °C, SS undergoes decomposition into coke, tar, moisture, and various light hydrocarbon gases. Simultaneously, a series of interactions among pyrolysis-related products occur as the temperature rises. For instance, tar cracking, steam gasification, and methane reforming happen in the initial stage. In the middle stage, the bonds of heat-resistant organic compounds break and undergo thermal cracking. Additionally, in the later stages, secondary thermal cracking, carbonization, and degradation of structurally stable organic components occur.²⁶ Importantly, because of the presence of endogenous Fe_2O_3 , which promoted catalytic pyrolysis at high temperatures, Fe_2O_3 could catalyze tar cracking to form more reducing gases, as shown in eqs 4–6.²⁷



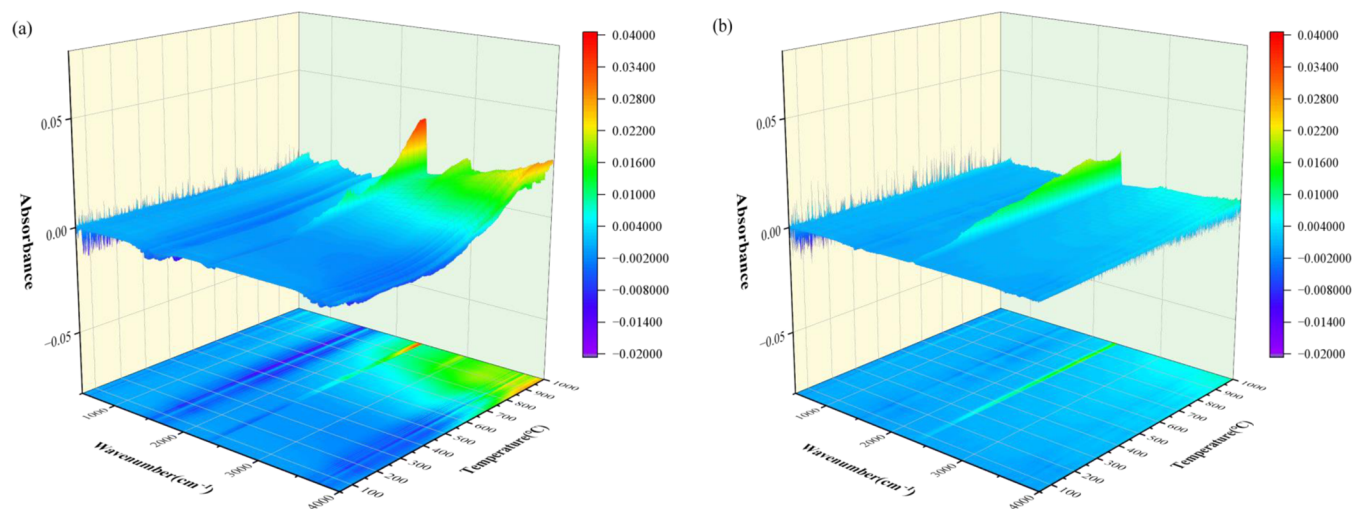
As the temperature surpasses 700 °C and enters the fourth stage, decomposition occurs in the inorganic minerals, leading to the formation of reconstituted minerals through a series of reactions involving the reducing gases produced by SS pyrolysis and iron-containing compounds. Under a reducing atmosphere, this can lead to the reduction of Fe_2O_3 and Fe_3O_4 to FeO, resulting in a loss of mass, as demonstrated in eqs 7–9.²⁸



As the reaction temperature rises, the sulfur present in the SS has the potential to be released as gas (SO_2) at approximately 750 °C. This can be attributed to the quick rate of temperature increase during the TG experiment, which could lead to thermal lag, thus causing the sulfur content to be liberated as SO_2 around 800–850 °C.²⁹ However, at the elevated temperature of 850 °C, CaO might interact chemically with

Table 2. Elemental Composition of SS at Different Decomposition Temperatures by XRF (Expressed as Oxides of Major Cations)

| end temperature (°C) | Fe ₂ O ₃ (wt %) | CaO (wt %) | P ₂ O ₅ (wt %) | SiO ₂ (wt %) | Al ₂ O ₃ (wt %) | SO ₃ (wt %) | K ₂ O (wt %) | Cl (wt %) |
|----------------------|---------------------------------------|------------|--------------------------------------|-------------------------|---------------------------------------|------------------------|-------------------------|-----------|
| 700 | 48.25 | 12.38 | 10.12 | 11.18 | 8.67 | 2.26 | 0.63 | 0.67 |
| 750 | 48.02 | 12.29 | 10.27 | 11.07 | 8.87 | 2.38 | 0.63 | 0.55 |
| 800 | 47.15 | 12.15 | 10.57 | 11.96 | 9.49 | 2.39 | 0.62 | 0.32 |
| 850 | 47.92 | 12.27 | 10.70 | 11.18 | 9.26 | 1.97 | 0.62 | 0.18 |
| 900 | 49.01 | 12.42 | 10.38 | 10.32 | 8.75 | 2.52 | 0.63 | 0.15 |

**Figure 2.** 3D infrared spectra of the FA and SS at 10 K/min: (a) TG-FTIR coupled gas-phase FTIR transform diagram of FA at wavenumber 500–4000 cm⁻¹ in the temperature range of 50–1000 °C. (b) TG-FTIR coupled gas-phase FTIR transform diagram of SS at wavenumber 500–4000 cm⁻¹ in the temperature range of 50–1000 °C.

SO₂, resulting in its solidification within the mineral. This phenomenon can be validated by the observable microgravity changes linked to thermal hysteresis, as reflected in the sulfur element migration pattern shown in Table 2.

3.1.2. Pyrolysis Microgravity TG-FTIR Analysis of Volatile Substance Release Characteristics. The three-dimensional (3D) FTIR spectra of the details of typical gas emission absorption peaks of SS and FA heat in the temperature range of 50–1000 °C are shown in Figure 2, which depicts the release of gaseous products in the wavelength range of 4000–500 cm⁻¹.

Figure 2a illustrates the FTIR spectral analysis of fly ash (FA). In the wavenumber range of 3170–3600 cm⁻¹, the presence of hydroxyl, H-bonded alcohols, or phenol stretching vibrations was observed.³⁰ As the temperature increased to 700 °C, there was an upsurge in the free radical •OH and potential oxidation of VOCs (olefins and aromatics) to nitrogen oxides, sulfur oxides, and halogenated compounds.³¹ When the temperature reached 600 °C, the wavenumber range of 2850–3100 cm⁻¹ signified the cracking and volatilization stage of hydrocarbons.³² Peaks in the wavenumber range of 2400–2240 cm⁻¹ were attributed to the cleavage and reformation of carboxyl and carbonyl functional groups at medium and high temperatures. As the temperature exceeded 830 °C, the infrared spectrum displayed a distinct peak, indicating CO₂ production, potentially marking the temperature threshold for efficient decomposition of carbonates.³³ Upon reaching 788.51 °C, CO₂ was produced through the decomposition of hydrocarbons and carbonates, which also resulted in the generation of CH₄ within the wavenumber

range of 2950–3016 cm⁻¹ and CO within the wavenumber range of 2060–2240 cm⁻¹ as gas-phase compounds.³⁴

Figure 2b shows that H₂O precipitated in the wavenumber range of 3500–4000 cm⁻¹ during the SS pyrolysis process. The generation of H₂O at 800 °C was mainly due to the material dehydroxylation reaction.³⁵ Generally, the main reaction mechanism in the wavenumber range 3100–2850 cm⁻¹ was summarized as the decomposition of macromolecular organics into organic molecules, which eventually convert to small molecules of hydrocarbons.³⁶ The peak was the wavenumber in the range 2400–2240 cm⁻¹, which was composed of two phases of CO₂ release. The first stage was dominated by the CO₂ products released from the pyrolysis of light organic matter. The second stage produced more CO₂ than the first stage, mainly because of the catalytic effect of the iron phase component on the decomposition and volatilization of the compounds within the SS at 800–850 °C.³⁷ This is consistent with the results of thermogravimetric experiments. As the reaction temperature exceeded 800 °C, CO₂ was released by pyrolysis, which greatly increased the chance of reduction reaction of CO₂ with iron-containing compounds having a catalytic effect. Owing to the catalysis of iron-containing compounds, some CO₂ was reduced to CO in the wavenumber range of 2400–2240 cm⁻¹.³⁸

3.1.3. Analysis of Catalytic Pyrolysis of Endogenous Iron in Sludge at High Temperatures. Owing to their thermal stability, iron compounds were enriched during pyrolysis in the SS-based biochar, which caused an increase in temperature. This section used XRD data analysis (Figure 6) to further clarify the catalytic effect of SS endogenous iron present in the pyrolysis process.³⁹ After high-temperature pyrolysis, the

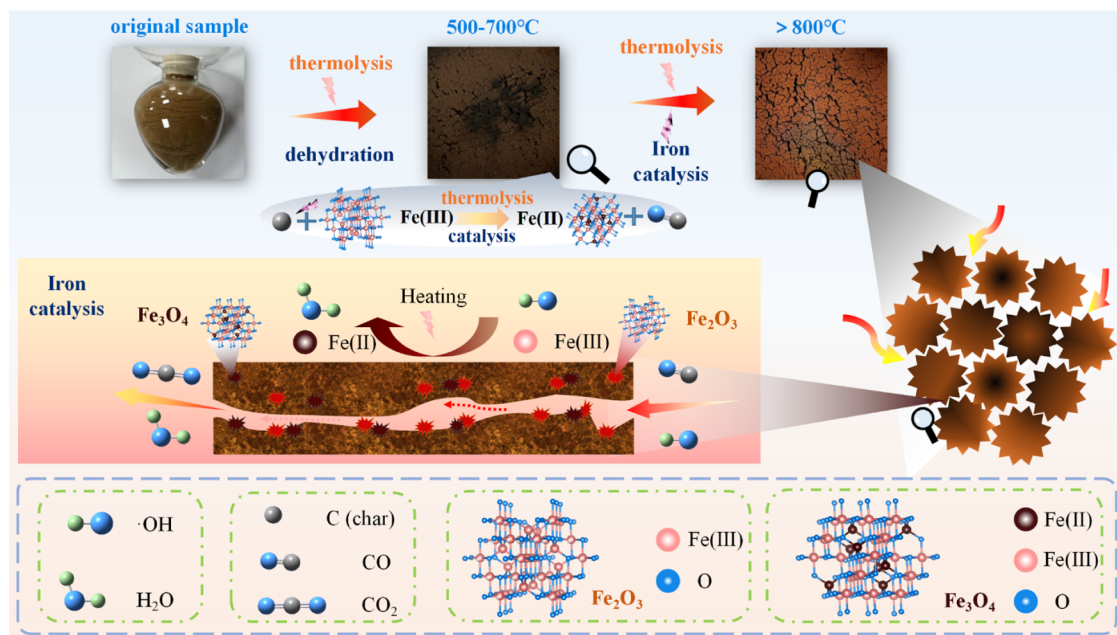


Figure 3. Endogenous catalytic mechanism of iron at high temperatures.

microchannel inside the SS-based biochar was washed away by the generated gas.³¹ Therefore, the surface and pores of the SS crystals provide more catalytic reaction sites for the enriched Fe_2O_3 and Fe_3O_4 .⁴⁰

At the same time, the high content of Fe catalysis in SS also promoted the formation of layered pore structures in the SS crystals. The formation of Fe_3O_4 and FeO was potentially the in situ thermal reduction of Fe_2O_3 by α -Fe due to amorphous carbon and reducing gas. The electrocatalytic oxidation of SS at the interface between SS flocs and particle electrodes can accelerate oxygen transfer during SS wall-breaking dehydration and enhance the formation of oxidative free radicals in the electric field.

As shown in Figure 3, the increase in temperature accelerated the redox reaction of Fe_2O_3 and organic biochar in the SS and catalyzed the production of more oxidative free radicals and CO. With the release of CO in the internal biochar, a complex pore structure was formed inside the SS, which showed that increase in pyrolysis temperature was beneficial to looser SS. With the reduction of organic biochar, the enrichment of inorganic metal oxides, represented by Fe-containing inorganic oxides, increased with the increase in pyrolysis temperature, which provided more catalytic sites to further induce the formation of oxidants (e.g., free radicals and CO) inside the SS. At the pyrolysis temperatures above 800 °C, Fe(III) in Fe_2O_3 is reduced to Fe(II) and exists in the form of Fe_3O_4 and FeO.

3.2. Co-Pyrolysis of SS and FA. **3.2.1. Synergetic Interaction Analysis.** The TG/DTG curves of SS, FA, and different ratios of their mixtures at a temperature rise rate of 10 K/min, where the pyrolysis temperature range was 50–1000 °C, are shown in Figure 4. It is clear that the TG curves of the mixtures were between those of SS and FA. However, owing to the different synergistic or inhibitory effects of the two at different ratios, the weight loss rate might be higher or lower than that of the raw DTG of SS and FA at different temperature bands. With the increase in FA in the mixtures, the overall trend of SS showed more volatile bound moisture,

easier decomposition oxidation of small-molecule components, and accelerated mass loss of the samples. Simultaneously, the CaCO_3 decomposition temperature point of the DTG curve gradually shifted forward as the percentage of FA gradually approximated that of SS owing to the increase in the percentage of FA. In addition, the TG curve of the mixture increased with increasing FA owing to the volatilization of sulfides and chlorides in the fourth stage.

When compared to FA alone, the mixture reached the maximum weight loss rate earlier. This was primarily due to the ongoing thermal decomposition of organic components in the SS and the combustion of coke. The latter process generated a significant amount of reactive radicals as a result of the thermal decomposition of small organic molecules within the SS. Moreover, the addition of FA further facilitated the decomposition of complex aromatic compounds. Thus, the inclusion of FA at an appropriate ratio bolstered the stability of SS pyrolysis while simultaneously mitigating the overall pyrolysis effect of the mixture. It is likely that FA leveraged the heat generated from the phase reaction of SS organic matter combustion for energy.⁴¹

The ΔW calculations provide a visual representation of the synergistic or inhibitory effects at various temperature points. A synergistic effect is represented by the red area above $\Delta W \geq 0$, indicating a positive interaction during the co-pyrolysis of SS and FA. Conversely, the blue area below $\Delta W < 0$ represents an inhibitory effect, indicating a negative interaction during co-pyrolysis. Notably, different blending ratios at different temperatures yielded varying synergistic or inhibitory effects.

According to Figure 4d, the co-pyrolysis of SS and FA at 85 and 90% blending ratios exhibited a synergistic effect. At a blending ratio of 95%, the co-pyrolysis conditions of SS and FA showed a suppression effect across the entire temperature range. As shown in Figure 4f, the co-pyrolysis of SS and FA at blending ratios of 70, 75, and 80% exhibited a synergistic effect within the temperature ranges of 50–675 and 825–924 °C. However, a co-pyrolysis inhibition effect was observed in the temperature range of 675–825 °C. This effect can be

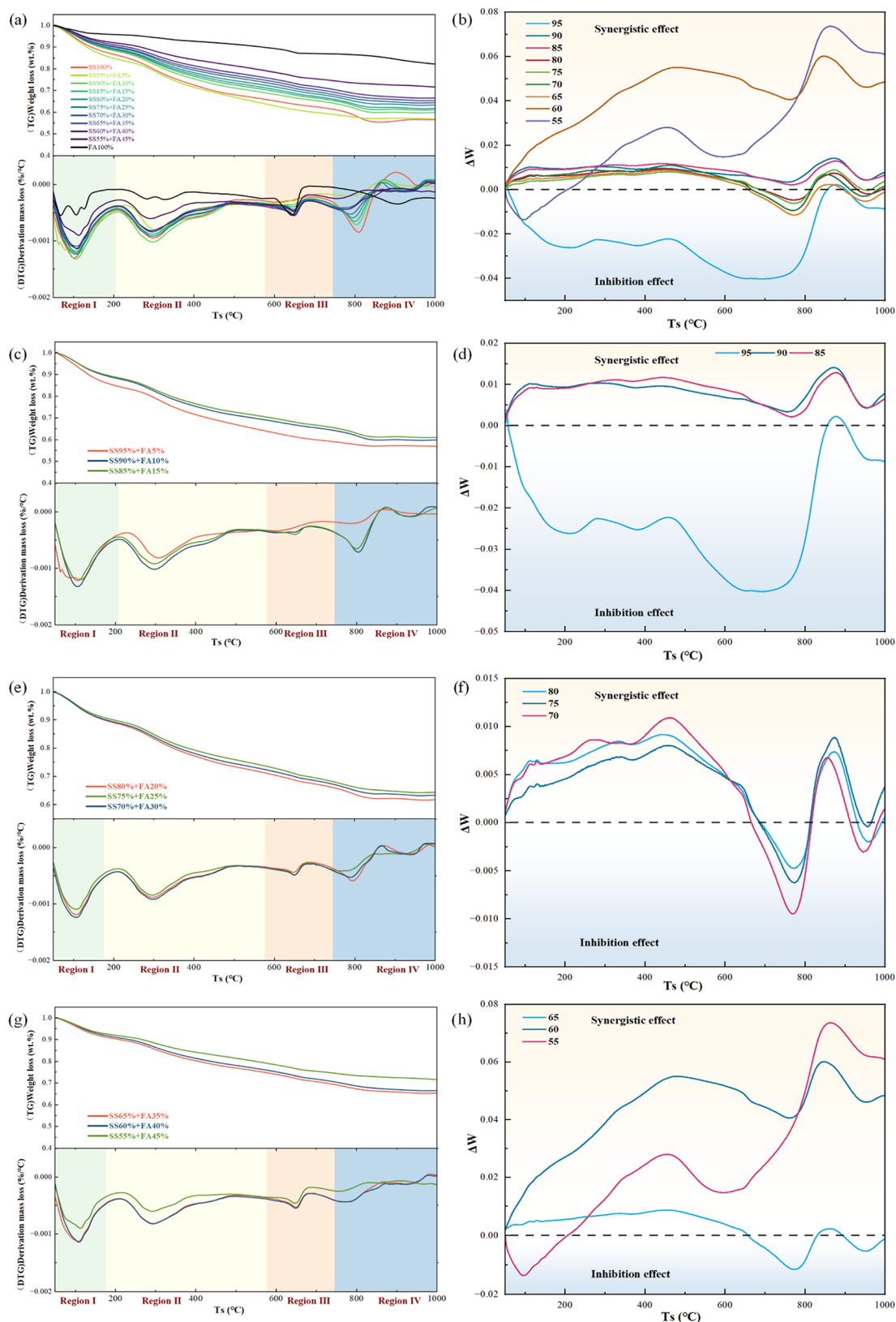
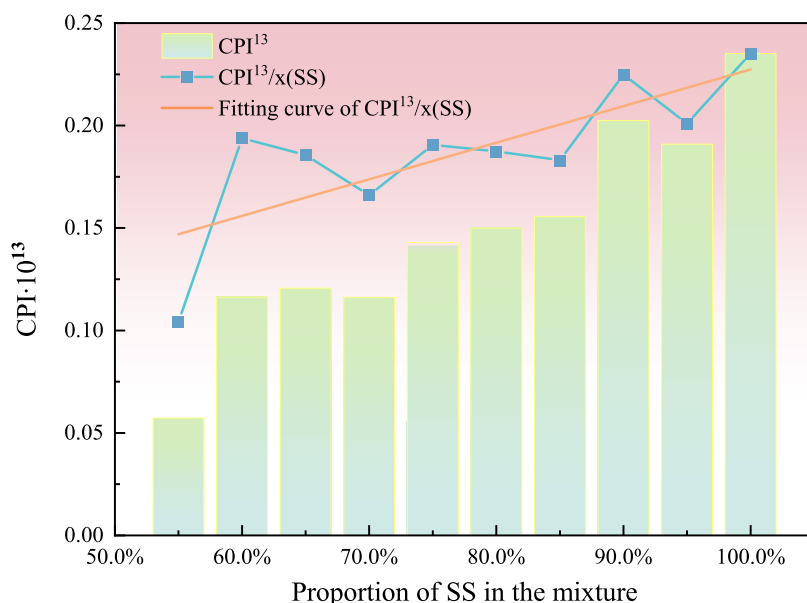


Figure 4. TG and DTG curves of SS, FA, and their corresponding blending samples at different mixing ratios exhibited synergistic or inhibitory effects of the mixtures when the pyrolysis temperature interval was 50–1000 °C at a heating rate of 10 K/min. (a) TG and DTG curves of SS, FA and their corresponding co-mixed samples at all mixing ratios of the experiment; (b) synergistic or inhibitory effects of SS, FA at all mixing ratios of the experiment; (c) TG and DTG curves of SS, FA, and SS at mixing ratios of 95, 90, and 85%; (d) synergistic or inhibitory effects of SS, FA, and SS at mixing ratios of 95, 90, and 85%; (e) TG and DTG curves at 80, 75, and 70% mixing ratios of SS, FA, and SS; (f) synergistic or inhibitory effects of SS, FA, and SS at mixing ratios of 80, 75, and 70%; (g) TG and DTG curves at 65, 60, and 55% mixing ratios of SS, FA, and SS; (h) synergistic or inhibitory effects of SS, FA, and SS at mixing ratios of 65, 60, and 55%.

Table 3. Characteristic Parameters of Pyrolysis at a Heating Rate of 10 K/min for Different Blending Ratios of SS and FA in the Temperature Interval of 50–1000 °C

| sample | $\Delta T_{1/2}$ (°C) | T_i (°C) | T_p (°C) | DTG _{max} (%/min) | DTG _{mean} (%/min) | M_∞ (%) | CPI $\times 10^{13}$ |
|---------------|-----------------------|------------|------------|----------------------------|-----------------------------|----------------|----------------------|
| SS(100%) | 220.63 | 210.71 | 298.08 | 0.0015 | 0.0005 | 43.45% | 0.2352 |
| SS95% + FA5% | 243.95 | 228.96 | 307.36 | 0.0019 | 0.0004 | 43.12% | 0.1909 |
| SS90% + FA10% | 219.36 | 201.81 | 296.61 | 0.0013 | 0.0005 | 40.89% | 0.2024 |
| SS85% + FA15% | 221.13 | 211.55 | 296.61 | 0.0012 | 0.00045 | 39.98% | 0.1556 |
| SS80% + FA20% | 220.31 | 210.61 | 297.12 | 0.0012 | 0.00045 | 38.28% | 0.1499 |
| SS75% + FA25% | 230.76 | 211.86 | 296.6 | 0.0012 | 0.00047 | 36.74% | 0.1429 |
| SS70% + FA30% | 226.54 | 210.61 | 297.87 | 0.0011 | 0.00042 | 35.75% | 0.1162 |
| SS65% + FA35% | 224.11 | 211.76 | 293.12 | 0.0011 | 0.00044 | 34.68% | 0.1207 |
| SS60% + FA40% | 224.37 | 211.84 | 293.96 | 0.0011 | 0.00044 | 33.57% | 0.1163 |
| SS55% + FA45% | 232.54 | 216.19 | 292.81 | 0.0009 | 0.00033 | 28.39% | 0.0573 |
| FA(100%) | 610.52 | 216.09 | 643.87 | 0.0005 | 0.0002 | 17.91% | 0.0021 |

**Figure 5.** Mixed pyrolysis index (CPI $\times 10^{13}$) for different FA and SS blending ratios and the combined pyrolysis index (CPI $\times 10^{13}/x$) per unit blending ratio at a heating rate of 10 K/min.

attributed to the presence of FA, specifically Al_2O_3 and SiO_2 , which inhibit the breakdown of long-chain hydrocarbons.⁴¹ Figure 4h indicates that co-pyrolysis conditions at a blending ratio of 60% for SS and FA showed a synergistic effect across the entire temperature range. However, the co-pyrolysis conditions at blending ratios of 55 and 65% for SS and FA exhibited inhibitory effects at 50–208 °C and 665–1000 °C, respectively. Based on these results, it can be concluded that blending ratios of 60, 85, and 90% for SS and FA demonstrated synergistic effects throughout the temperature range. Exceptionally, when the blending ratio was 60%, the synergistic characterization amount W could exceed 0.06, indicating a significantly higher synergistic effect of pyrolysis compared to blending ratios of 85 and 90%.

This might have occurred because SS and FA can provide different promotions at different stages of pyrolysis. In the first stage, the organic matter in SS was encouraged to dewater along with FA, which has alkalinity because SS has a large amount of Fe(III) and can be employed as a skeletal material to enhance SS dewatering.⁴² In the second stage, it could be that the organic matter within the SS combines with the halogenated elements within the FA, thus showing a synergistic drive. In the third stage, it might be that the decomposition of

CaCO_3 in FA is accelerated by Fe_2O_3 catalysis, leading to a forward shift in its decomposition temperature.⁴³ The fourth stage is probably the efficient catalytic decomposition of complex compounds by Fe(II) and Fe(III) with the reconstituted volatilization of S and Cl elements with metal cations.⁴¹ Carbon reduction of iron oxides dominated the reaction, which consumed large amounts of carbon-containing organic complex compounds and released large amounts of carbon dioxide at temperatures above 700 °C.⁴⁴

3.2.2. Pyrolysis Performance Parameters. To better describe the pyrolysis properties of SS under the influence of different blending ratios of FA, several parameters of the pyrolysis properties obtained from the TG-DTG curves are presented in Table 3. With the increase of the FA blending ratio from 0 to 45%, the pyrolysis composite devolatilization index $\text{CPI} \times 10^{13}$ of the mixed samples showed a decreasing trend.

The free radical reaction of SS and FA influenced thermal decomposition, and the thermal stability of the halogen compounds of FA led to the decomposition of the mixture, generating primary radicals and intermediates. The source of light-rich hydrocarbons may be volatilized owing to the presence of iron in the SS. Because the presence of iron

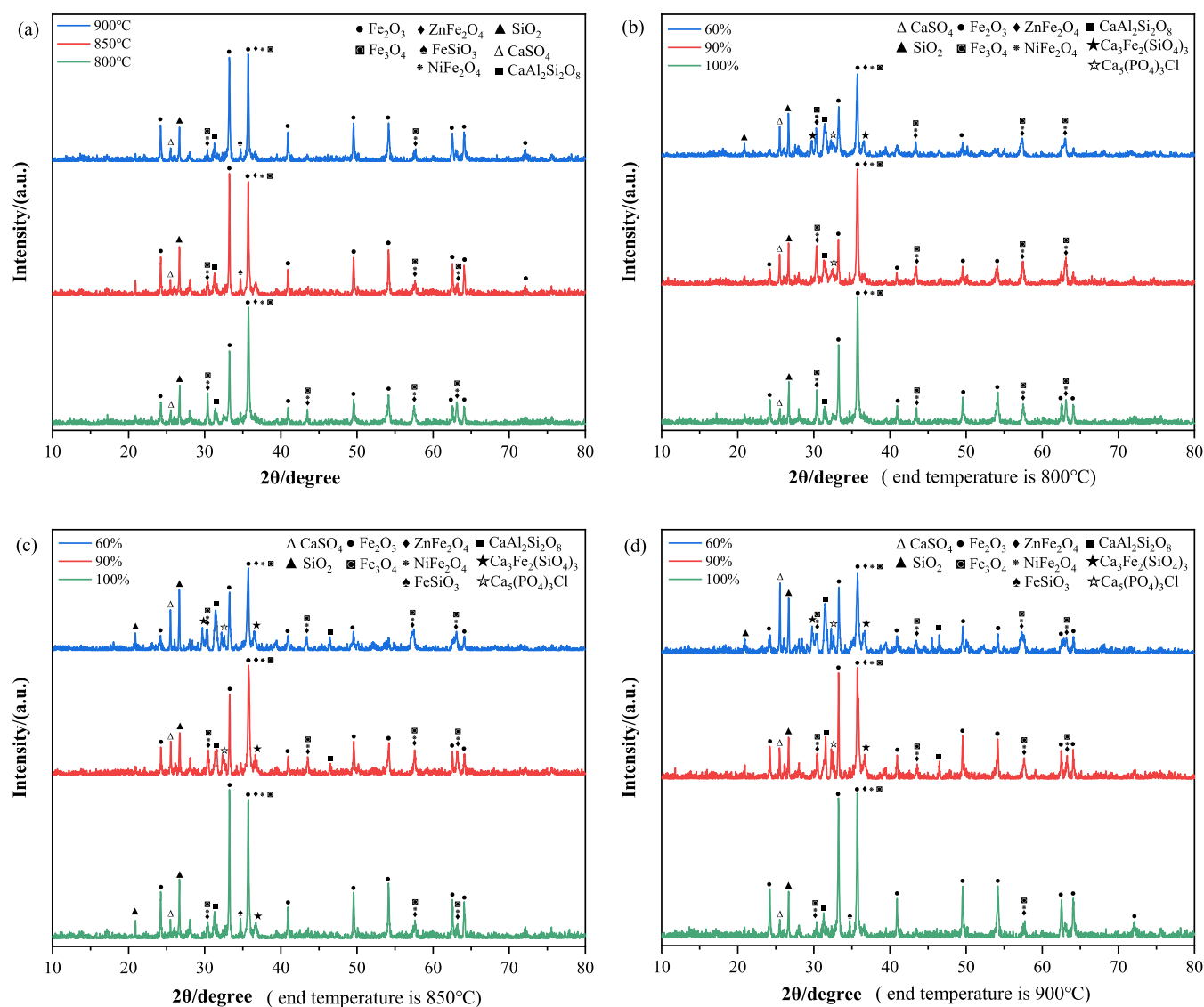


Figure 6. Structural changes of samples in the temperature interval of 800–900 °C. (a) Mineral phase variation of pure SS samples with temperature, (b) mineral facies change with different mixing amounts at 800 °C, (c) mineral facies change with different mixing amounts at 850 °C, and (d) mineral facies change with different mixing amounts at 900 °C.

promoted the formation of complex minerals from simple minerals, the iron phase within the SS accelerated the solidification of heavy metals in the FA by polymerizing at high temperatures (Section 3.3.2). However, considering that the percentage of inorganic components in the sample increases with adding FA, the $\text{CPI} \times 10^{13}$ of the sample pyrolysis process would decrease. Therefore, to verify the effect of FA on SS embodied by pyrolysis promotion, it is observed that the unit $\text{CPI} \times 10^{13}$ of SS at the current blending ratio is required to characterize its rise. Mixed pyrolysis index ($\text{CPI} \times 10^{13}$) data is shown in Figure 5.

By fitting the $\text{CPI} \times 10^{13}$ values, it was found that the overall trend of the integrated pyrolysis index increased with an increase in the municipal SS blending amount for a constant total amount of pyrolysis. However, the $\text{CPI} \times 10^{13}$ values were above the fitted curve at 60, 65, 75, and 90% of SS blending, indicating better pyrolysis performance at these blending ratios.

Combined with the synergistic characterization analysis of SS and FA and the evaluation of the comprehensive index of

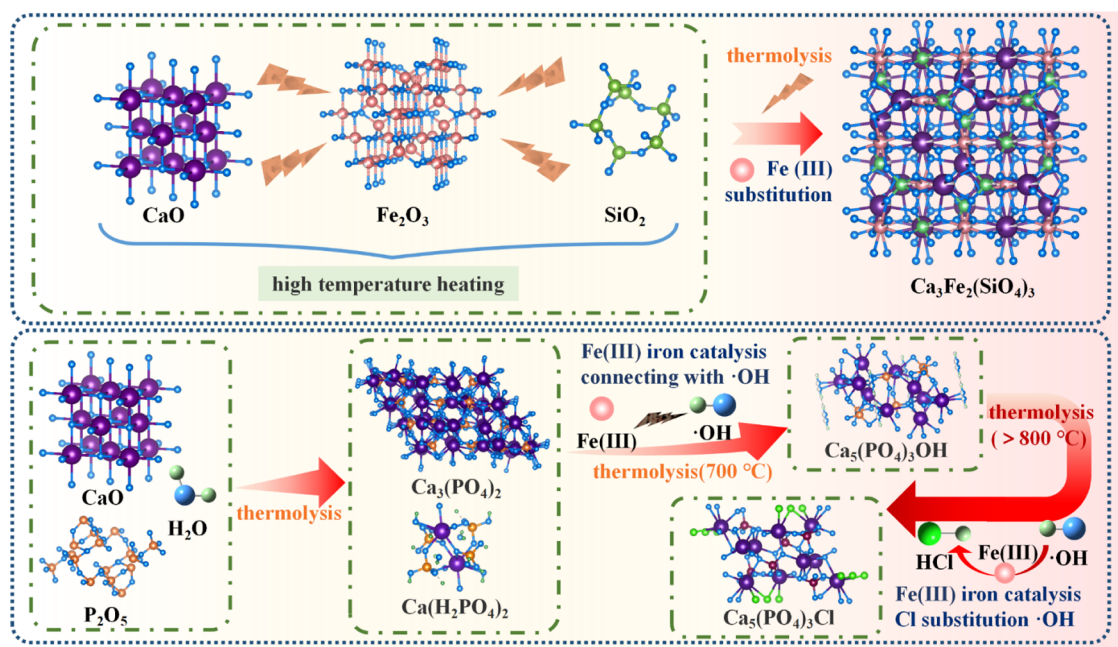
pyrolysis, it was found that the two blending ratios of 60 and 90% were the most favorable for the pyrolysis reaction, and the interactive promotion effect of both parties was most obvious at this stage.

3.3. Mineral Phase Transformation. **3.3.1. Mineral Phase Transformation at Different Temperatures with Dominant Blending Ratios.** The effects of deposition temperature and FA co-mixing on the evolution of the mineral crystal phase were further evaluated by X-ray diffraction (XRD) analysis. Figure 6 shows the XRD analysis results of FA deposition at different temperatures, demonstrating the evolution of the main crystalline phases in the SS and FA (at 60 and 90% blending ratios).

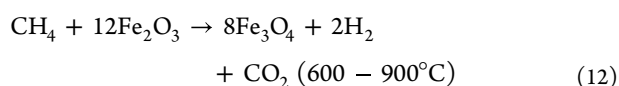
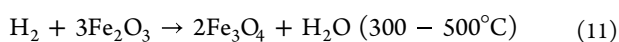
As shown in Figure 6a, Fe₂O₃ was identified as the dominant crystalline phase in the deposit within the temperature range of 800–900 °C, and its abundance gradually increased with rising temperature. Although elemental Fe in the SS pyrolysis residues primarily existed as Fe₂O₃, it was inferred that the Fe species present in the pyrolysis environment were Fe(II) and FeO, as depicted in eqs 10–12. This phenomenon could

Table 4. Elemental Composition (Expressed as Oxides of Major Cations) of SS with FA at Optimal Ratios in the Temperature Interval of 800–900 °C Determined by XRF

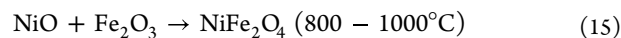
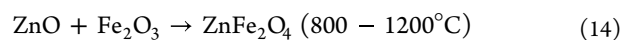
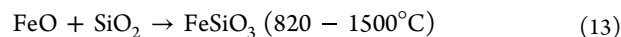
| ratio SS/FA | end temp. (°C) | Fe ₂ O ₃ (wt %) | CaO (wt %) | SiO ₂ (wt %) | P ₂ O ₅ (wt %) | Al ₂ O ₃ (wt %) | SO ₃ (wt %) | K ₂ O (wt %) | Cl (wt %) |
|-------------|----------------|---------------------------------------|------------|-------------------------|--------------------------------------|---------------------------------------|------------------------|-------------------------|-----------|
| 9/1 | 800 | 45.4 | 16.5 | 12.8 | 9.23 | 8.58 | 3.91 | 0.88 | 1.08 |
| | 850 | 45.2 | 16.4 | 13.1 | 9.82 | 9.09 | 3.38 | 0.83 | 0.71 |
| | 900 | 45.6 | 16.7 | 12.4 | 10.1 | 8.61 | 3.61 | 0.73 | 0.69 |
| 6/4 | 800 | 28.9 | 24.4 | 18.5 | 6.05 | 9.89 | 5.24 | 2.64 | 1.35 |
| | 850 | 29.1 | 24.2 | 18.1 | 7.18 | 9.83 | 4.94 | 2.48 | 1.37 |
| | 900 | 29.1 | 24.8 | 18.7 | 6.76 | 9.71 | 5.18 | 2.43 | 1.13 |

**Figure 7.** Analysis of endogenous polymerization mechanism of iron at high temperatures.

be attributed to the potential reaction of reducing substances (CO, H₂, CH₄) generated during SS pyrolysis with the initial Fe₂O₃ content in the SS, forming iron-containing species with lower valence states. On the other hand, SiO₂, Fe₃O₄, ZnFe₂O₄, and NiFe₂O₄ displayed a gradual decline in the temperature range of 800–900 °C. Around 850 °C, the compounds containing Fe(II) reacted with SiO₂ to form FeSiO₃. Additionally, the presence of CaAl₂Si₂O₈ and CaSO₄ was observed in the deposited samples at temperatures ranging from 800 to 900 °C. Moreover, the intensity of the diffraction peaks increased with the deposition temperature, indicating a higher abundance of the iron phase. Therefore, it can be inferred that iron phase catalysis might have facilitated the sulfation of calcium in the high-temperature environment.^{45,46} Furthermore, it was found that, at a specific temperature, Fe(II) and Fe(III) could form amorphous crystals within the aluminosilicate structure. However, beyond 800 °C, the iron phase displayed polymeric characteristics as it interacted with other compounds, resulting in binding.



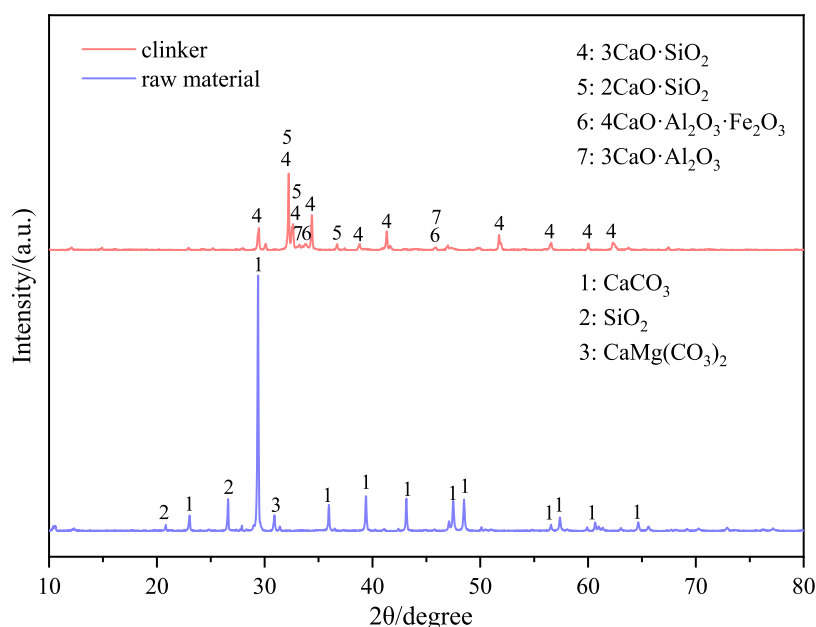
As shown in eqs 13 and 14, the high-temperature anoxic environment was accompanied by some FeO, which increased the composition of the mineral phase toward FeSiO₃. The substitution of CaO with SiO₂ led to the substitution of Ca(II) with Fe(II).⁴⁷ Owing to the high iron content of the SS sample, the increase in Fe₂O₃, replacing Al₂O₃ combined with Zn(II) led to the substitution of Al(III) by Fe(III). As shown in eq 15, Ni is an iron-loving element, and when the temperature reaches certain conditions, the heavy nickel in the SS polymerizes with Fe₂O₃, and Ni can be successfully solidified.⁴⁸



As shown in Figure 6b–d, two new polymeric minerals, Ca₃Fe₂(SiO₄)₃ and Ca₅(PO₄)₃Cl, were formed inside the mixture with FA incorporation. Moreover, when the pyrolysis end-temperature conditions were the same, the diffraction peaks of the mineral Ca₅(PO₄)₃Cl were significantly enhanced with an increase in the proportion of FA. After FA incorporation, the mineral Ca₃Fe₂(SiO₄)₃ formation started at 800 °C when the blending ratio of FA and SS was 4:6. At the same blending ratio, the diffraction peaks of mineral Ca₃Fe₂(SiO₄)₃ showed an enhanced trend with an increase in the pyrolysis temperature. Owing to the high CaO and SiO₂

Table 5. XRF Analysis of the Elemental Composition of Raw Material and Clinker with SS and FA in Participating Pairings

| samples | CaO (wt %) | SiO ₂ (wt %) | Al ₂ O ₃ (wt %) | Fe ₂ O ₃ (wt %) | MgO (wt %) | K ₂ O (wt %) | TiO ₂ (wt %) | P ₂ O ₅ (wt %) |
|----------|------------|-------------------------|---------------------------------------|---------------------------------------|------------|-------------------------|-------------------------|--------------------------------------|
| raw meal | 73.22 | 13.03 | 5.69 | 5.41 | 1.60 | 0.59 | 0.24 | 0.06 |
| clinker | 67.33 | 22.62 | 3.87 | 3.15 | 2.03 | 0.61 | 0.19 | 0.07 |

**Figure 8.** XRD analysis of the elemental composition of raw material and clinker with SS and FA in participating pairings.

contents of FA, the diffraction peaks of CaSO_4 and SiO_2 showed a significant enhancement trend at different pyrolysis end-temperatures as the blending amount of FA increased. Furthermore, the diffraction peaks of CaSO_4 and SiO_2 reached their highest peak value when the final temperature of pyrolysis reached 900°C . As can be seen from Table 4, the mixed samples showed an increase in elemental S content after 900°C compared with 850°C at different blending ratios of SS and FA. Consistent with the pure SS material, the law confirms that iron phase catalysis might favor the sulfation of calcium in a high-temperature environment.^{46,49} The XRD analysis indicated that the incorporation of FA resulted in high-temperature volatile elements (such as S, Cl, and P), which were originally inside the FA and successfully solidified in the minerals by the polymerization catalytic effect of iron in the SS.

From the above discussion, it could be concluded that the iron phase compounds could significantly enhance the stabilization of heavy metals in the co-pyrolysis biochar and contribute to the increase in the admixture ratio of FA in the FA/SS mixture. The reason for the enhanced effect might be due to the aggregation of Fe(II) and Fe(III) in the FA/SS mixture. During this period, Fe(II) and Fe(III) were converted to Fe-containing minerals. In a high-temperature environment, the conversion of Fe ions led to the formation of certain heavy metals through the interaction of Fe-containing minerals. This process effectively hindered the release of heavy metals from pyrolysis carbon. Therefore, it was crucial to analyze and investigate the role of iron in mineral solidification as a facilitator of aggregation.

3.3.2. Polymerization Reaction of Endogenous Iron Compounds in Sludge at High Temperatures. It was found that when SS and FA are mixed, the heavy metals in the mixture were successfully solidified at high temperatures.

Compared to pure SS, the mixed samples formed a complex mixture of $\text{Ca}_3\text{Fe}_2(\text{SiO}_4)_3$ and $\text{Ca}_5(\text{PO}_4)_3\text{Cl}$ at high temperatures, which might be due to the endogenous polymerization effect of iron in SS.

As depicted in Figure 7, a sequence of reactions occur with the rise in temperature. At 500°C , the CaO in the FA reacts with P_2O_5 and H_2O , resulting in the formation of $\text{Ca}_3(\text{PO}_4)_2$ and $\text{Ca}(\text{H}_2\text{PO}_4)_2$. When the temperature escalates to 700°C , the iron present in the SS catalyzes the free radical oxidation, leading to the production of $\text{Ca}_5(\text{PO}_4)_3\text{OH}$. Upon reaching 800°C , the Cl element within the FA transforms into the form of HCl. Consequently, at this pyrolysis temperature, the $\text{Ca}_5(\text{PO}_4)_3\text{OH}$ in the mixed sample undergoes iron catalysis, giving rise to the evolution of phosphorus-bound minerals. These minerals lose free radicals to react with HCl, generating $\text{Ca}_5(\text{PO}_4)_3\text{Cl}$, as outlined in eq 16.

In the case of blending with CaO-rich FA, the mineral $\text{Ca}_3\text{Fe}_2(\text{SiO}_4)_3$ is produced, and its diffraction peak intensity amplifies with the increment in FA content. This compound has a complex composition, represented by the formula $\text{A}_3\text{B}_2[\text{SiO}_4]_3$, where A could represent divalent cations such as Mg(II), Fe(II), Mn(II), or Ca(II), and B may be Al(III), Fe(III), Cr(III), or Ti(IV). The radii of the trivalent cations in the compound are comparable, permitting isomorphous substitution among them. However, the situation differs for the divalent ions. Specifically, Ca(II) has a larger radius compared to Mg(II), Fe(II), and Mn(II), which complicates isomorphous substitution.⁵⁰ Therefore, as indicated in eq 17, $\text{Ca}_3\text{Fe}_2(\text{SiO}_4)_3$ is an easily formed, stable mineral in the presence of adequate sources of calcium and iron. The unique structural characteristics of the $\text{A}_3\text{B}_2[\text{SiO}_4]_3$ compound class mean that the divalent cation Ca(II) with its large atomic radius is not readily replaced by other divalent iron ions.

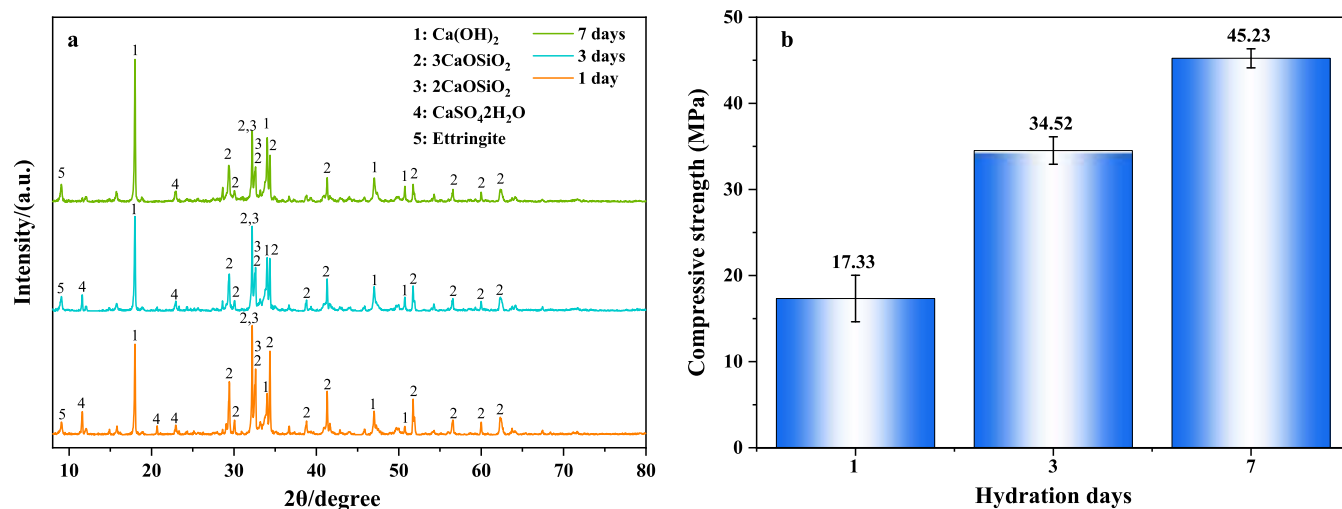
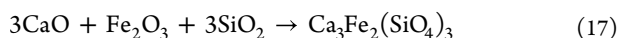
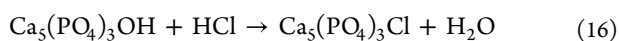


Figure 9. Characteristic analysis of Portland cement mixed with SS and FA after hydration. (a) XRD mineral analysis and (b) compressive strength performance test.

Table 6. ICP Experimental Results of Heavy-Metal Leaching from Portland Cement Blended with SS and FA

| hydration (days) | Zn (mg/L) | Cu (mg/L) | Mn (mg/L) | Ni (mg/L) | As (mg/L) | Pb (mg/L) | Cr (mg/L) | Cd (mg/L) |
|------------------|-----------|-----------|-----------|-----------|-----------|-----------|-----------|-----------|
| 1 | 0 | 0 | 0 | 0.007 | 0.064 | 0 | 0.08 | 0 |
| 3 | 0 | 0 | 0 | 0 | 0.049 | 0 | 0.052 | 0 |
| 7 | 0 | 0 | 0 | 0 | 0.04 | 0 | 0.036 | 0 |

Nevertheless, in an SS environment, an abundance of Fe(III) creates favorable conditions for atomic substitution.



In summary, the SS could be initially solidified with heavy metals by blending FA for synergistic mineralization to comprehensively utilize high-iron ore resources.

3.3.3. Cement Kiln Application of Predisposed SS and FA Involved in the Production of Portland Cement. To increase the co-processing of solid waste in cement kilns, this study proposes a detailed implementation plan for actual Portland cement production. SS and FA undergo preheating and are integrated with cement raw materials via tertiary air mixing inside the kiln. A novel buffer warehouse employing an SMP system belt conveyor is introduced to effectively incorporate pre-processed SS and FA into the kiln tail calciner. Additionally, we adopt a multilayer airlock configuration that includes two layers of flap valves and two layers of plate valves. This setup is designed to mitigate any potential adverse effects on the kiln's performance that may arise from a loose airlock. The blended formula, incorporating SS and FA in proportions equivalent to 100 tons of raw meal content, is used to manufacture 2500 tons/day of Portland cement clinker. The compositions of raw material and clinker, when blended with SS and FA, are outlined in Table 5, while the corresponding mineral X-ray diffraction (XRD) analysis is demonstrated in Figure 8.

The XRD mineral analysis indicated that the primary mineral compositions of the raw materials were CaCO_3 , SiO_2 , and CaMgCO_3 , accounting for 83.9, 9.5, and 6.6%, respectively, as determined through quantitative analysis. After calcination in the cement kiln, the XRD mineral analysis revealed that the predominant mineral components of the

clinker were $3\text{CaO}\cdot\text{SiO}_2$ and $2\text{CaO}\cdot\text{SiO}_2$, comprising 48.3 and 38.7%, respectively. These compositions met the requirements for the preparation of Portland cement. A posthydration strength test was conducted to assess the effect of SS and FA in the mixture on cement strength. The cement blocks (dimension: 2 cm × 2 cm × 2 cm) were first prepared by solid-phase mixing of clinker and gypsum in the ratio of 95:5% and then with a water-to-cement ratio of 0.29. Compressive strength was measured at 1, 3, and 7 days and compared to that of standard Portland cement. Finally, the hydrated minerals were analyzed by XRD for the corresponding days, and the outcomes are presented in Figure 9.

The XRD analysis (shown in Figure 9a) indicated that the peak intensity of $\text{Ca}(\text{OH})_2$ increased significantly with prolonged hydration time, suggesting a corresponding increase in content. Conversely, the peak intensities of $3\text{CaO}\cdot\text{SiO}_2$, $2\text{CaO}\cdot\text{SiO}_2$, and $\text{CaSO}_4\cdot 2\text{H}_2\text{O}$ decreased, while the peak intensity of calcium aluminate showed a slight increase during this period. The compressive strength test (depicted in Figure 9b) indicated that the compressive strengths of Portland cement at the 1-day, 3-day, and 7-day marks were 17.33, 34.52, and 45.23 MPa, respectively. After 3 days of hydration, the compressive strength of the Portland cement sample exceeded the 32 MPa compressive strength index requirement of the Chinese National Standard GB 175-2007 62.5R, suggesting that an appropriate blend of SS and FA was beneficial to the early strength of Portland cement.

To investigate the solidification effect of SS and FA following synergistic pretreatment in Portland cement, a heavy-metal ion leaching test was conducted in accordance with the national standard GB/T 30810. Table 6 shows the ICP results, indicating that only three heavy-metal ions, namely, Ni, As, and Cr, were leached after the hydration of Portland cement. Importantly, the leaching rate of these ions gradually decreased as the hydration time increased. By

comparing these outcomes with those defined by the Chinese national standard GB 30760-2014, it was discovered that the maximum leaching values were lower than the maximum limits of Ni (0.2 mg/L), As (0.1 mg/L), and Cr (0.2 mg/L). This demonstrated the solidification of heavy-metal ions during the Portland cement production process after the synergistic pretreatment of SS and FA.

4. CONCLUSIONS

Compositional and thermal characterization of raw solid waste samples uncovered the intricate synergistic relationships inherent to the post-mixing thermal treatment process. Experiments involving proportional blending via thermogravimetric (TG) analysis revealed a synergistic pyrolysis process across the temperature range of 50–1000 °C. This occurred when the ratio of SS to FA was 6:4 or 9:1. The data thus suggests that iron within the SS has a positive catalytic effect on pyrolysis in a high-temperature anoxic environment. This facilitates the accelerated removal of harmful VOCs from the SS. Moreover, the endogenous polymerization impact of Fe during the synthesis of minerals with adequate Fe supply can lower the reaction activation energy and promote the formation of complex minerals. Heavy metals and toxic compounds, such as S and Cl, are available for synergistic solidification under the catalytic influence of iron sources with the addition of FA to supply calcium and silicon sources. In summary, a properly blended addition of FA allows for the thorough elimination of hazardous organic components from SS, and the solidification of heavy metals and toxic elements, thereby enhancing its use in cement kilns.

In terms of SS, its high water and organic matter content pose challenges for its direct use as a cement replacement material, similar to other cementitious materials. Its potential applications are further restricted by its relatively low SiO₂, Al₂O₃, and CaO content compared to FA. The presence of elemental impurities like chlorine, sulfur, and phosphorus in FA, as identified in this study, can induce corrosion. Leveraging the iron in SS to encourage the predegradation of hazardous solid waste could alleviate the risk to cement kilns during the co-processing of FA and SS. In a compelling test, 100 tons of pre-processed SS was blended daily with FA in a 2500 tons per day Portland cement production line, according to the material ratio. The resulting Portland cement achieved a compressive strength of 34.52 MPa after just 3 days of hydration, pointing toward a promising potential for raw material substitution in cement production.

■ ASSOCIATED CONTENT

SI Supporting Information

The Supporting Information is available free of charge at <https://pubs.acs.org/doi/10.1021/acsomega.3c03586>.

Hazards of supplementing phosphorus in iron-rich sewage sludge; XRD analysis of experimental raw materials in supplementary; XRF test analysis of SS after each temperature treatment; co-processing process of HOTDISC for the co-processing of a cement kiln; comprehensive pyrolysis index (CPI); and possible reactions during the SS pyrolysis (PDF)

■ AUTHOR INFORMATION

Corresponding Author

Yanpeng Mao – National Engineering Laboratory for Reducing Emissions from Coal Combustion, Engineering Research Center of Environmental Thermal Technology of Ministry of Education, Shandong Key Laboratory of Energy Carbon Reduction and Resource Utilization, School of Energy and Power Engineering, Shandong University, Jinan, Shandong 250061, China; orcid.org/0000-0003-1306-6845; Phone: +86 531 88399372; Email: maoyanpeng@sdu.edu.cn; Fax: +86 531 88395877

Authors

Dongjie Pang – National Engineering Laboratory for Reducing Emissions from Coal Combustion, Engineering Research Center of Environmental Thermal Technology of Ministry of Education, Shandong Key Laboratory of Energy Carbon Reduction and Resource Utilization, School of Energy and Power Engineering, Shandong University, Jinan, Shandong 250061, China

Yang Jin – National Engineering Laboratory for Reducing Emissions from Coal Combustion, Engineering Research Center of Environmental Thermal Technology of Ministry of Education, Shandong Key Laboratory of Energy Carbon Reduction and Resource Utilization, School of Energy and Power Engineering, Shandong University, Jinan, Shandong 250061, China

Jiazheng Zhang – National Engineering Laboratory for Reducing Emissions from Coal Combustion, Engineering Research Center of Environmental Thermal Technology of Ministry of Education, Shandong Key Laboratory of Energy Carbon Reduction and Resource Utilization, School of Energy and Power Engineering, Shandong University, Jinan, Shandong 250061, China

Jingyi Dong – Beijing Ciroten Environmental Protection Technology Co., Ltd., Beijing 100070, China

Xujiang Wang – National Engineering Laboratory for Reducing Emissions from Coal Combustion, Engineering Research Center of Environmental Thermal Technology of Ministry of Education, Shandong Key Laboratory of Energy Carbon Reduction and Resource Utilization, School of Energy and Power Engineering, Shandong University, Jinan, Shandong 250061, China

Jingwei Li – National Engineering Laboratory for Reducing Emissions from Coal Combustion, Engineering Research Center of Environmental Thermal Technology of Ministry of Education, Shandong Key Laboratory of Energy Carbon Reduction and Resource Utilization, School of Energy and Power Engineering, Shandong University, Jinan, Shandong 250061, China

Wenlong Wang – National Engineering Laboratory for Reducing Emissions from Coal Combustion, Engineering Research Center of Environmental Thermal Technology of Ministry of Education, Shandong Key Laboratory of Energy Carbon Reduction and Resource Utilization, School of Energy and Power Engineering, Shandong University, Jinan, Shandong 250061, China; orcid.org/0000-0002-6346-3614

Complete contact information is available at: <https://pubs.acs.org/doi/10.1021/acsomega.3c03586>

Notes

The authors declare no competing financial interest.

ACKNOWLEDGMENTS

The authors gratefully acknowledge the financial support from the National Key Research Development Program of China (2020YFC1910000) and the Key Research Development Project of Shandong Province (2022CXGC010701).

REFERENCES

- (1) Zuloaga, O.; Navarro, P.; Bizkarguenaga, E.; Iparraguirre, A.; Vallejo, A.; Olivares, M.; Prieto, A. Overview of extraction, clean-up and detection techniques for the determination of organic pollutants in sewage sludge: A review. *Anal. Chim. Acta* **2012**, *736*, 7–29.
- (2) (a) Liu, J.; Zhuo, Z.; Xie, W.; Kuo, J.; Lu, X.; Buyukada, M.; Evrendilek, F. Interaction effects of chlorine and phosphorus on thermochemical behaviors of heavy metals during incineration of sulfur-rich textile dyeing sludge. *Chem. Eng. J.* **2018**, *351*, 897–911. (b) Chen, M.; Oshita, K.; Takaoka, M.; Shiota, K. Co-incineration effect of sewage sludge and municipal solid waste on the behavior of heavy metals by phosphorus. *Waste Manage.* **2022**, *152*, 112–117.
- (3) (a) Liew, C.-S.; Kiatkittipong, W.; Lim, J.-W.; Lam, M.-K.; Ho, Y.-C.; Ho, C.-D.; Ntwampe, S. K. O.; Mohamad, M.; Usman, A. Stabilization of heavy metals loaded sewage sludge: Reviewing conventional to state-of-the-art thermal treatments in achieving energy sustainability. *Chemosphere* **2021**, *277*, No. 130310. (b) Khawer, M. U. B.; Naqvi, S. R.; Ali, I.; Arshad, M.; Juchelková, D.; Anjum, M. W.; Naqvi, M. Anaerobic digestion of sewage sludge for biogas & biohydrogen production: State-of-the-art trends and prospects. *Fuel* **2022**, *329*, No. 125416.
- (4) (a) Ali, I.; Tariq, R.; Naqvi, S. R.; Khoja, A. H.; Mehran, M. T.; Naqvi, M.; Gao, N. Kinetic and thermodynamic analyses of dried oily sludge pyrolysis. *J. Energy Inst.* **2021**, *95*, 30–40. (b) Sorinolu, A. J.; Tyagi, N.; Kumar, A.; Munir, M. Antibiotic resistance development and human health risks during wastewater reuse and biosolids application in agriculture. *Chemosphere* **2021**, *265*, No. 129032.
- (5) (a) Soria-Verdugo, A.; Kauppinen, J.; Soini, T.; Garcia-Gutiérrez, L. M.; Pikkariainen, T. Pollutant emissions released during sewage sludge combustion in a bubbling fluidized bed reactor. *Waste Manage.* **2020**, *105*, 27–38. (b) Zhong, M.; Yang, D.; Liu, R.; Ding, Y.; Dai, X. Effects of hydrothermal treatment on organic compositions, structural properties, dewatering and biogas production of raw and digested sludge. *Sci. Total Environ.* **2022**, *848*, No. 157618. (c) Han, H.; Li, A.; Zhu, M.; Hu, S.; Xu, J.; Xiong, Z.; Ren, Q.; Wang, Y.; Jiang, L.; Su, S.; Xiang, J. Heavy tar evolution characteristics during advanced sludge pyrolysis and biomass gasification integrated process. *Sci. Total Environ.* **2022**, *853*, No. 158107.
- (6) (a) Wang, X.; Wei-Chung Chang, V.; Li, Z.; Song, Y.; Li, C.; Wang, Y. Co-pyrolysis of sewage sludge and food waste digestate to synergistically improve biochar characteristics and heavy metals immobilization. *Waste Manage.* **2022**, *141*, 231–239. (b) Zhan, X.; Wang, L.; Gong, J.; Deng, R.; Wu, M. Co-stabilization/solidification of heavy metals in municipal solid waste incineration fly ash and electrolytic manganese residue based on self-bonding characteristics. *Chemosphere* **2022**, *307*, No. 135793.
- (7) Sobik-Szołtysek, J.; WYSTALSKA, K. Coprocessing of Sewage Sludge in Cement Kiln. In *Industrial and Municipal Sludge*; Prasad, M. N. V.; de Campos Favas, P. J.; Vithanage, M.; Mohan, S. V., Eds.; Butterworth-Heinemann, 2019; pp 361–381.
- (8) Valderrama, C.; Granados, R.; Cortina, J. L.; Gasol, C. M.; Guillem, M.; Josa, A. Comparative LCA of sewage sludge valorisation as both fuel and raw material substitute in clinker production. *J. Cleaner Prod.* **2013**, *51*, 205–213.
- (9) (a) Chang, J.-S.; Cho, Y.-C.; Lin, Y.-P. Regeneration of heavy metal contaminated soils for cement production by cement kiln co-processing. *Resour., Conserv. Recycl.* **2022**, *176*, No. 105909. (b) Gameda, T. N.; Melaku, Y. T.; Chamada, T. A.; Adugna, A. T. Optimization mixing ratio of the brewery waste water sludge and coal as energy source for cement industry and fuel ash effect on the raw material composition. *Environ. Chall.* **2022**, *7*, No. 100476.
- (10) (a) Da, Y.; He, T.; Shi, C. Unveiling the cooperation effects of fluorine and copper on tricalcium silicate (C₃S) during cement kiln co-processing hazardous wastes containing Cu. *Constr. Build. Mater.* **2022**, *337*, No. 127612. (b) Kumarasamy, K.; Doss, M. V. S.; Anand, A. V. Evaluation of thermo mechanical and corrosion properties of uniaxially pressed refractory blocks used in the transition zone of cement rotary kilns. *Mater. Today: Proc.* **2022**, *64*, 455–458.
- (11) Pang, D.; Mao, Y.; Jin, Y.; Song, Z.; Wang, X.; Li, J.; Wang, W. Review on the use of sludge in cement kilns: mechanism, technical, and environmental evaluation. *Process Saf. Environ. Prot.* **2023**, *172*, 1072–1086.
- (12) (a) Mujumdar, K. S.; Ganesh, K. V.; Kulkarni, S. B.; Ranade, V. V. Rotary Cement Kiln Simulator (RoCKS): Integrated modeling of pre-heater, calciner, kiln and clinker cooler. *Chem. Eng. Sci.* **2007**, *62*, 2590–2607. (b) Ma, X.; Shao, W.; Cui, Z. Energy and thermodynamic analysis of a typical cement production system based on experimental and simulated investigations. *Case Stud. Therm. Eng.* **2022**, *38*, No. 102357. (c) Okoji, A. I.; Anozie, A. N.; Omoleye, J. A.; Taiwo, A. E.; Osuolale, F. N. Energetic assessment of a precalcining rotary kiln in a cement plant using process simulator and neural networks. *Alex. Eng. J.* **2022**, *61*, 5097–5109. (d) Okoji, A. I.; Anozie, A. N.; Omoleye, J. A. Evaluating the thermodynamic efficiency of the cement grate clinker cooler process using artificial neural networks and ANFIS. *Ain Shams Eng. J.* **2022**, *13*, No. 101704.
- (13) Clavier, K. A.; Ferraro, C. C.; Townsend, T. G. Pilot-scale cement production using treated waste incineration bottom ash: physical and environmental performance. *Resour., Conserv. Recycl.* **2021**, *175*, No. 105862.
- (14) Pant, B.; Ojha, G. P.; Kim, H.-Y.; Park, M.; Park, S.-J. Fly-ash-incorporated electrospun zinc oxide nanofibers: Potential material for environmental remediation. *Environ. Pollut.* **2019**, *245*, 163–172.
- (15) Seo, M.; Lee, S. Y.; Lee, C.; Cho, S. S. Recycling of Cement Kiln Dust as a Raw Material for Cement. *Environments* **2019**, *6*, No. 113.
- (16) Liu, J.; Wang, Z.; Xie, G.; Li, Z.; Fan, X.; Zhang, W.; Xing, F.; Tang, L.; Ren, J. Resource utilization of municipal solid waste incineration fly ash - cement and alkali-activated cementitious materials: A review. *Sci. Total Environ.* **2022**, *852*, No. 158254.
- (17) (a) Andruschak, S. V.; Besedin, P. V.; Doroganov, E. A. Modeling the transportation and batching of slurry into a cement kiln. *IOP Conf. Ser.: Mater. Sci. Eng.* **2019**, *560*, No. 012139. (b) Trinh, M. M.; Chang, M. B. Catalytic pyrolysis: New approach for destruction of POPs in MWIs fly ash. *Chem. Eng. J.* **2021**, *405*, No. 126718.
- (18) Cerbo, A. A. V.; Ballesteros, F.; Chen, T. C.; Lu, M. C. Solidification/stabilization of fly ash from city refuse incinerator facility and heavy metal sludge with cement additives. *Environ. Sci. Pollut. Res.* **2017**, *24*, 1748–1756.
- (19) Chen, Z.; Yu, G.; Wang, Y.; Wang, X. Fate of heavy metals during co-disposal of municipal solid waste incineration fly ash and sewage sludge by hydrothermal coupling pyrolysis process. *Waste Manage.* **2020**, *109*, 28–37.
- (20) Hu, Y.; Yang, F.; Chen, F.; Feng, Y.; Chen, D.; Dai, X. Pyrolysis of the mixture of MSWI fly ash and sewage sludge for co-disposal: Effect of ferrous/ferric sulfate additives. *Waste Manage.* **2018**, *75*, 340–351.
- (21) Xiao, H.; Li, K.; Zhang, D.; Tang, Z.; Niu, X.; Yi, L.; Lin, Z.; Fu, M. Environmental, energy, and economic impact assessment of sludge management alternatives based on incineration. *J. Environ. Manage.* **2022**, *321*, No. 115848.
- (22) (a) Zhang, J.; Liu, J.; Evrendilek, F.; Zhang, X.; Buyukada, M. TG-FTIR and Py-GC/MS analyses of pyrolysis behaviors and products of cattle manure in CO₂ and N₂ atmospheres: Kinetic, thermodynamic, and machine-learning models. *Energy Convers. Manage.* **2019**, *195*, 346–359. (b) Sun, H.; Bi, H.; Jiang, C.; Ni, Z.; Tian, J.; Zhou, W.; Qiu, Z.; Lin, Q. Experimental study of the co-pyrolysis of sewage sludge and wet waste via TG-FTIR-GC and artificial neural network model: Synergistic effect, pyrolysis kinetics and gas products. *Renewable Energy* **2022**, *184*, 1–14.

- (23) Ai, Z.; Zhang, W.; Yang, L.; Chen, H.; Xu, Z.; Leng, L.; Li, H. Investigation and prediction of co-pyrolysis between oily sludge and high-density polyethylene via in-situ DRIFTS, TGA, and artificial neural network. *J. Anal. Appl. Pyrolysis* **2022**, *166*, No. 105610.
- (24) Ren, P.; Ling, T.-C. Roles of chlorine and sulphate in MSWIFA in GGBFS binder: Hydration, mechanical properties and stabilization considerations. *Environ. Pollut.* **2021**, *284*, No. 117175.
- (25) Bravo, P. M.; Jimenez, R.; Devred, F.; Debecker, D. P.; Ulloa, C.; Garcia, X. Kinetics of CO methanation using a Fe-bearing catalyst from a blast furnace sludge. *Fuel* **2020**, *276*, No. 118045.
- (26) Chen, J.; Fang, H.; Xu, F.; Ren, Y.; Wang, Z.; Zhu, Y.; Mu, L. Influence of iron-containing petrochemical sludge ash on the pyrolysis of pine wood: Thermal behaviors, thermodynamic analysis, and kinetic parameters. *Bioresour. Technol.* **2022**, *345*, No. 126551.
- (27) Leion, H.; Jerndal, E.; Steenari, B.-M.; Hermansson, S.; Israelsson, M.; Jansson, E.; Johnsson, M.; Thunberg, R.; Vadenbo, A.; Mattisson, T.; Lyngfelt, A. Solid fuels in chemical-looping combustion using oxide scale and unprocessed iron ore as oxygen carriers. *Fuel* **2009**, *88*, 1945–1954.
- (28) Wan, Q.; Liu, Y.; Guo, Q.; Tian, A. Influence of Shenmu Coal Ash on the Reaction Characteristics and Structure of Fe-based Oxygen Carrier in Coal Char Chemical Looping Gasification. *Chin. J. Process Eng.* **2017**, *17*, 995–1001.
- (29) Huang, Z.; He, F.; Zhao, K.; Zhao, G.; Shi, H.; Li, H. Natural hematite oxygen carriers for chemical-looping gasification of biomass. *Trans. Chin. Soc. Agric. Eng.* **2011**, *27*, 105–111.
- (30) Gao, N.; Sipra, A. T.; Quan, C. Thermogravimetric analysis and pyrolysis product characterization of municipal solid waste using sludge fly ash as additive. *Fuel* **2020**, *281*, No. 118572.
- (31) Lin, K.-H.; Hsu, H.-T.; Ko, Y.-W.; Shieh, Z.-X.; Chiang, H.-L. Pyrolytic product characteristics of biosludge from the wastewater treatment plant of a petrochemical industry. *J. Hazard. Mater.* **2009**, *171*, 208–214.
- (32) Mo, W.; Wu, Z.; He, X.; Qiang, W.; Wei, B.; Wei, X.; Wu, Y.; Fan, X.; Ma, F. Functional group characteristics and pyrolysis/combustion performance of fly ashes from Karamay oily sludge based on FT-IR and TG-DTG analyses. *Fuel* **2021**, *296*, No. 120669.
- (33) Fernández, J. R.; Abanades, J. C. CO₂ capture from the calcination of CaCO₃ using iron oxide as heat carrier. *J. Cleaner Prod.* **2016**, *112*, 1211–1217.
- (34) Gu, Q.; Wu, W.; Jin, B. Investigation of thermal characteristics of municipal solid waste incineration fly ash under various atmospheres: A TG-FTIR study. *Thermochim. Acta* **2019**, *681*, No. 178402.
- (35) Yu, H.; Zhang, D.; Gu, L.; Wen, H.; Zhu, N. Coupling sludge-based biochar and electrolysis for conditioning and dewatering of sewage sludge: Effect of char properties. *Environ. Res.* **2022**, *214*, No. 113974.
- (36) Xu, T.; Wang, C.; Hong, D.; Li, S.; Yue, S. The synergistic effect during co-combustion of municipal sludge and coal: Experimental and ReaxFF molecular dynamic study. *Energy* **2023**, *262*, No. 125553.
- (37) Fuentes, I.; Bernales, N.; Ulloa, C.; García, X. Kinetics of CO₂ methanation using a Fe-bearing blast furnace sludge as catalytic precursor. *Catal. Today* **2022**, *394–396*, 198–207.
- (38) Xiao, Y.; Zeng, J.-F.; Liu, J.-W.; Lu, X.; Shu, C.-M. Reactive force field (ReaxFF) molecular dynamics investigation of bituminous coal combustion under oxygen-deficient conditions. *Fuel* **2022**, *318*, No. 123583.
- (39) Xia, S.; Yang, H.; Lei, S.; Lu, W.; Cai, N.; Xiao, H.; Chen, Y.; Chen, H. Iron salt catalytic pyrolysis of biomass: Influence of iron salt type. *Energy* **2023**, *262*, No. 125415.
- (40) Mu, K.; Zhang, Q.; Luo, G.; Han, J.; Qin, L.; Zhao, B.; Chen, W.; Yi, L. Role of iron conditioners on organics evolution in overall process of sludge hydrothermal carbonization followed by pyrolysis. *Renewable Energy* **2022**, *198*, 169–175.
- (41) Lin, F.; Zheng, F.; Li, J.; Sun, B.; Che, L.; Yan, B.; Chen, G. Catalytic pyrolysis of oily sludge with iron-containing waste for production of high-quality oil and H₂-rich gas. *Fuel* **2022**, *326*, No. 124995.
- (42) Xu, Z.-X.; Song, H.; Deng, X.-Q.; Zhang, Y.-Y.; Xue-Qin, M.; Tong, S.-Q.; He, Z.-X.; Wang, Q.; Shao, Y.-W.; Hu, X. Dewatering of sewage sludge via thermal hydrolysis with ammonia-treated Fenton iron sludge as skeleton material. *J. Hazard. Mater.* **2019**, *379*, No. 120810.
- (43) Li, J.; Zheng, F.; Li, Q.; Farooq, M. Z.; Lin, F.; Yuan, D.; Yan, B.; Song, Y.; Chen, G. Effects of inherent minerals on oily sludge pyrolysis: Kinetics, products, and secondary pollutants. *Chem. Eng. J.* **2022**, *431*, No. 133218.
- (44) Zhu, J.; Lin, S.; Fan, Y.; Chen, Y.; Jin, L.; Gao, H. Investigations on the iron-rich textile dyeing sludge pyrolysis characteristics: Thermal decomposition behaviors, products, potential mechanisms. *J. Anal. Appl. Pyrolysis* **2023**, *169*, No. 105834.
- (45) Qian, L.; Yan, S.; Yong, X.; Selvaraj, M.; Ghramh, H. A.; Assiri, M. A.; Zhang, X.; Awasthi, M. K.; Zhou, J. Effective degradation of chloramphenicol in wastewater by activated peroxymonosulfate with Fe-rich porous biochar derived from petrochemical sludge. *Chemosphere* **2022**, *310*, No. 136839.
- (46) Su, L. L.; Li, R. J.; Huang, N.; Zhu, T. T.; Deng, S. H.; Wang, X. X.; Yang, G.; Zhang, Y. Z.; Long, L. L. The silicon active sites driven by oxygen vacancies in iron silicate for activating peroxymonosulfate. *J. Colloid Interface Sci.* **2022**, *628*, 955–965.
- (47) Liu, T.; Wen, C.; Zhou, K.; Li, C.; Zhu, Y.; Wang, D.; Li, R.; Jing, Z. Influence of collaborative disposal of sewage sludge in the fly ash partitioning and PM10 emission from a subcritical coal-fired boiler. *Fuel* **2023**, *331*, No. 125871.
- (48) Li, M.; Su, P.; Guo, Y.; Zhang, W.; Mao, L. Effects of SiO₂, Al₂O₃ and Fe₂O₃ on leachability of Zn, Cu and Cr in ceramics incorporated with electroplating sludge. *J. Environ. Chem. Eng.* **2017**, *5*, 3143–3150.
- (49) Ai, J.; Wang, Z.; Dionysiou, D. D.; Liu, M.; Deng, Y.; Tang, M.; Liao, G.; Hu, A.; Zhang, W. Understanding synergistic mechanisms of ferrous iron activated sulfite oxidation and organic polymer flocculation for enhancing wastewater sludge dewaterability. *Water Res.* **2021**, *189*, No. 116652.
- (50) Kong, L. B.; Liu, L.; Yang, Z.; Li, S.; Zhang, T.; Wang, C. Theory of Ferrimagnetism and Ferrimagnetic Metal Oxides. In *Magnetic, Ferroelectric, and Multiferroic Metal Oxides*; Stojanovic, B. D., Ed.; Elsevier, 2018; pp 287–311.